Opto-Electronic
Advances

CN 51−1781/TN ISSN 2096−4579 (Print) ISSN 2097−3993 (Online)

Embedded solar adaptive optics telescope: achieving compact integration for high-efficiency solar observations

Naiting Gu, Hao Chen, Ao Tang, Xinlong Fan, Carlos Quintero Noda, Yawei Xiao, Libo Zhong, Xiaosong Wu, Zhenyu Zhang, Yanrong Yang, Zao Yi, Xiaohu Wu, Linhai Huang and Changhui Rao

Citation: Gu NT, Chen H, Tang A, et al. Embedded solar adaptive optics telescope: achieving compact integration for high-efficiency solar observations. *Opto-Electron Adv* **8**, 250025(2025).

https://doi.org/10.29026/oea.2025.250025

Received: 16 February 2025; Accepted: 21 April 2025; Published online: 27 May 2025

Related articles

High-resolution visible imaging with piezoelectric deformable secondary mirror: experimental results at the 1.8-m adaptive telescope

Youming Guo, Kele Chen, Jiahui Zhou, Zhengdai Li, Wenyu Han, Xuejun Rao, Hua Bao, Jinsheng Yang, Xinlong Fan, Changhui Rao

Opto-Electronic Advances 2023 **6**, 230039 doi: 10.29026/oea.2023.230039

More related article in Opto-Electronic Journals Group website

Opto-Electronic Advances

Article

May 2025, Vol. 8, No. 5

DOI: 10.29026/oea.2025.250025 CSTR: 32247.14.oea.2025.250025

Embedded solar adaptive optics telescope: achieving compact integration for high-efficiency solar observations

Naiting Gu[1*], Hao Chen[2,3], Ao Tang[2,3,4], Xinlong Fan[2,3], Carlos Quintero Noda[5,6], Yawei Xiao[2,3,4], Libo Zhong[2,3], Xiaosong Wu[2,3,4], Zhenyu Zhang[3], Yanrong Yang[7], Zao Yi[8], Xiaohu Wu[9*], Linhai Huang[2,3,4*] and Changhui Rao[2,3,4*]

Adaptive optics (AO) has significantly advanced high-resolution solar observations by mitigating atmospheric turbulence. However, traditional post-focal AO systems suffer from external configurations that introduce excessive optical surfaces, reduced light throughput, and instrumental polarization. To address these limitations, we propose an embedded solar adaptive optics telescope (ESAOT) that intrinsically incorporates the solar AO (SAO) subsystem within the telescope's optical train, featuring a co-designed correction chain with a single Hartmann-shack full-wavefront sensor (HS f-WFS) and a deformable secondary mirror (DSM). The HS f-WFS uses temporal-spatial hybrid sampling technique to simultaneously resolve tip-tilt and high-order aberrations, while the DSM performs real-time compensation through adaptive modal optimization. This unified architecture achieves symmetrical polarization suppression and high system throughput by minimizing optical surfaces. A 600 mm ESAOT prototype incorporating a 12×12 micro-lens array HS f-WFS and 61-actuator piezoelectric DSM has been developed and successfully conducted on-sky photospheric observations. Validations including turbulence simulations, optical bench testing, and practical observations at the Lijiang observatory collectively confirm the system's capability to maintain about $\lambda/10$ wavefront error during active region tracking. This architectural breakthrough of the ESAOT addresses long-standing SAO integration challenges in solar astronomy and provides scalability analyses confirming direct applicability to the existing and future large solar observation facilities.

Keywords: embedded solar adaptive optics telescope (ESAOT); hartmann-shack full-wavefront sensor (HS f-WFS); deformable secondary mirror (DSM); high-resolution solar observations; solar telescopes

Gu NT, Chen H, Tang A et al. Embedded solar adaptive optics telescope: achieving compact integration for high-efficiency solar observations. *Opto-Electron Adv* **8**, 250025 (2025).

[1]College of Advanced Interdisciplinary Studies, National University of Defense Technology, Changsha 410073, China; [2]National Laboratory on Adaptive Optics, Chengdu 610209, China; [3]Institute of Optics and Electronics, Chinese Academy of Sciences, Chengdu 610209, China; [4]University of Chinese Academy of Sciences, Beijing 101408, China; [5]Departanmento de Astrofísica, Univ. De La Laguna, La Laguna, Tenerife E-38025, Spain; [6]Instituto de Astrofísica de Canarias, La Laguna, Tenerife E-38025, Spain; [7]Chengdu University of Traditional Chinese Medicine, Chengdu 610075, China; [8]Joint Laboratory for Extreme Conditions Matter Properties, Southwest University of Science and Technology, Mianyang 621010, China; [9]Thermal Science Research Center, Shandong Institute of Advanced Technology, Jinan 250100, China.

*Correspondence: NT Gu, E-mail: gnt7328@163.com; XH Wu, E-mail: xiaohu.wu@iat.cn; LH Huang, E-mail: hlhai@ioe.ac.cn; CH Rao, E-mail: chrao@ioe.ac.cn

Received: 16 February 2025; Accepted: 21 April 2025; Published online: 27 May 2025

Introduction

The pursuit of solar magnetism understanding, initiated by Galileo's sunspot observations and revolutionized by Hale's discovery of sunspot magnetic fields[1], now confronts unprecedented challenges in resolving sub-arcsecond dynamics of the Sun's magnetic carpet. Recent breakthroughs such as direct evidence of solar active regions[2], large-scale magnetohydrodynamic oscillations in sunspots[3], and transverse oscillations in strongly magnetized regions observed with the 1.6 m Goode solar telescope (GST)[4] highlight the transformative role of high-resolution observations. These advancements challenge traditional views of wave-mediated energy transfer and address critical questions, such as coronal heating[5,6]. Discoveries like fast plasmoid-mediated reconnection in solar flares[7], solar magnetic field mapping from the photosphere to the base of the corona[8], solar prominence/filament paradox[9], high-resolution simulations of solar differential rotation[10] and reconnection-driven energy cascade in magnetohydrodynamic turbulence[11] further underscore the synergy between observational and theoretical progress. Crucially, such data underpin space weather modeling[12,13] and climate studies[14], necessitating next-generation telescopes to resolve finer solar features[15–17].

To achieve this, large-aperture solar telescopes (>1 m) are indispensable. Facilities like DKIST (4 m)[18], GST (1.6 m)[19,20], GREGOR (1.5 m)[15,21], CLST (1.8 m)[22,23], NVST (1 m)[24], and upcoming projects (EST (4 m)[25], CGST (8 m)[26,27], WeHot (2.5 m)[28], NLST[29] exemplify this trend. However, atmospheric turbulence limits their effective resolution to that of 10–20 cm apertures. Solar adaptive optics (SAO) systems mitigate this by real-time wavefront measurement and correction, enabling near-diffraction-limited imaging[30–32]. For instance, GREGOR's GAOS256 system[31], GST's AO308 system[33,34], NVST's 151-actuator SAO system[35–37], CLST's 451-actuator SAO system[22], and DKIST's 1600-actuator SAO system[38] demonstrate remarkable success in photospheric and chromospheric studies. Upcoming projects, including EST, WeHot, CGST, and NLST, similarly prioritize high-order SAO integration. To address the severe daytime atmospheric turbulence affecting solar observations, SAO has achieved remarkable advancements in high-speed wavefront sensing and real-time wavefront processing for low-contrast extended targets[39–41]. Despite advances in solar adaptive optics, conventional systems are still constrained by inherent limitations: optical relaying between different apertures of deformable mirror (DM), tip-tilt mirror (TTM), wavefront sensor (WFS), and fine-tracking sensors complicates the optical system, decreasing the transmittance and increasing the stray light, which decreases the signal-to-noise ratio; instrumental polarization due to multiple asymmetric reflections hampers precision magnetic field measurements; and reliability problems increase as telescope size increases due to intricate opto-mechanical configurations. Efforts to simplify AO integration have drawn inspiration from nighttime telescopes, where deformable secondary mirrors (DSMs) such as those in the multiple mirror telescope (MMT)[42–44], the large binocular telescope (LBT)[45–47], very large telescope (VLT)[48,49] replace discrete correctors and relay optics. While DSMs have simplified optical systems in nighttime telescopes by reducing relay optics, voice coil actuator (VCA) in these DSMs suffer from low bandwidth, thermal instability, large actuator size, low displacement resolution (micron-scale) and nonlinear hysteresis, restricting them to low spatio-temporal frequency corrections[50,51]. In contrast, piezoelectric ceramic actuator (PZT)-based DSMs overcome these challenges with kHz-range bandwidth, nanometer-scale precision, high actuator density and negligible thermal drift, making them promising alternatives[52]. While piezoelectric-actuated DSMs took ground-based night-time telescopes to a new level, the direct application of the same approach to solar astronomy inadvertently perpetuates systemic limitations due to the paradigm differences between AO and SAO including 1) wavefront sensing limitations based on low-contrast extended target; and 2) global tip-tilt detection challenges-a capability inherently unavailable in SAO due to extended target geometries. Specifically, the conventional framework which segregates tip-tilt correction (handled by a fast-steering mirror paired with a fine tracking sensor) and high-order wavefront control (managed via a deformable mirror, DM and a Hartmann-shack wavefront sensor, HS WFS) forces cascaded relay optics and oblique-incidence mirrors into solar instruments. This still complicates solar observing instruments and produces significant instrumental polarization, which is not conducive to high-sensitivity detection of the solar magnetic field. The Hartmann-shack wavefront sensor (HS WFS) captures high-order aberrations in extended solar targets but fails to detect global tip-tilt errors —a capability routinely achieved for stellar point sources in nighttime astronomy, causing irreversible loss of fixed and objective reference positions for extended targets when cross-correlation processes between sub-aperture images. Consequently, SAO systems generally uses separate fine-tracking sensor and fast-steering mirror, making it difficult to simplify the system further, even with DSMs.

To address these challenges, we propose an innovative embedded solar adaptive optics telescope (ESAOT) architecture that fundamentally re-configures wavefront correction paradigms for solar observation. The system integrates a piezoelectric-actuated concave ellipsoidal deformable secondary mirror (DSM) with a unified Hartmann-shack full-wavefront sensor (HS f-WFS), embedding solar adaptive optics (SAO) system directly within the telescope's optical path and enabling co-optimized wavefront correction through hardware-software co-design. Our temporal-spatial hybrid sampling methodology enables concurrent measurement of tip-tilt errors and high-order optical aberrations across extended solar features (e.g., sunspots and granulation patterns), compensated in real-time by a concave elliptical DSM. This integrated approach achieves structure simplification by eliminating fine-tracking sensors and fast-steering mirrors (FSM) while enhancing polarization symmetry and photo efficiency. Comprehensive validation encompasses turbulence simulations, optical bench verification, and field observations using our developed 600 mm aperture ESAOT prototype, marking the first successful implementation of embedded SAO technology. The ESAOT architecture achieves structural simplicity, high optical throughput, and minimized instrument-induced polarization while preserving real-time correction efficiency, addressing critical limitations in conventional SAO systems. The demonstrated method provides a cost-effective framework for next-generation solar telescopes, particularly promising for large-aperture facilities requiring high-precision polarization preservation.

Materials and methods

ESAOT architecture

The ESAOT architecture represents a significant advancement in solar telescope design, offering enhanced performance through innovative components and streamlined configurations. Specifically, it replaces the conventional secondary mirror near the exit pupil of the solar telescope with a piezoelectric-actuated DSM. This DSM is capable of real-time correction of wavefront aberrations across various spatial and temporal frequencies, including those caused by atmospheric turbulence.

To further optimize the system, a full-wavefront measurement method based on a Hartmann-shack sensor has been implemented. This method enables the simultaneous measurement of both global tip-tilt and higher-order wavefront aberrations using a single cross-correlation Hartmann-shack wavefront sensor (HS WFS). In this context, "tip-tilt wavefront aberration" describes the low-order wavefront error induced by angular deviations (tip/tilt) of the optical beam, whereas "high-order wavefront aberration" refers to wavefront errors with spatial frequencies beyond the tip-tilt component, encompassing defocus, astigmatism, comma, and higher-order terms. Corrections are then applied by the elliptical DSM. These innovations bring substantial benefits, including system simplification, increased transmission efficiency, and reduced instrumental polarization.

As shown in Fig. 1, compared to traditional solar telescopes, the co-design philosophy of the ESAOT architecture eliminates the need for separate tip-tilt mirrors and precision tracking subsystems. This approach achieves polarization purity by minimizing optical asymmetry, with the tip-tilt correction being strategically allocated between a Hexapod platform and a DSM based on temporal frequency characteristics. Specifically, the Hexapod compensates for low-frequency tip-tilt errors (primarily mechanical vibrations and thermal drift), while the DSM handles high-frequency errors. This dual-stage correction architecture effectively addresses major disturbance sources including wind loading, atmospheric turbulence, and structural vibrations. Moreover, the DSM's extended actuator stroke enables significantly greater angular correction range compared to conventional deformable mirrors (DMs). The reflective mirrors prior to the imaging camera are reduced from over eight to just two, thereby increasing system transmission from 48.4% to ≥86.5% (assuming a mirror reflectivity of 93% per surface with protected Ag/Al coatings in the imaging spectral band). This corresponds to a 1.8-fold improvement in total optical throughput. Additionally, the relay optics required to adapt the DM and HS WFS are no longer necessary, significantly simplifying the overall configuration of solar telescopes.

The core operational principle of ESAOT wavefront correction is schematically depicted in Fig. 1(c). A Hartmann-shack full-wavefront sensor (HS f-WFS) is employed to measure wavefront aberrations in the incident light. These aberrations are transmitted in real time to a

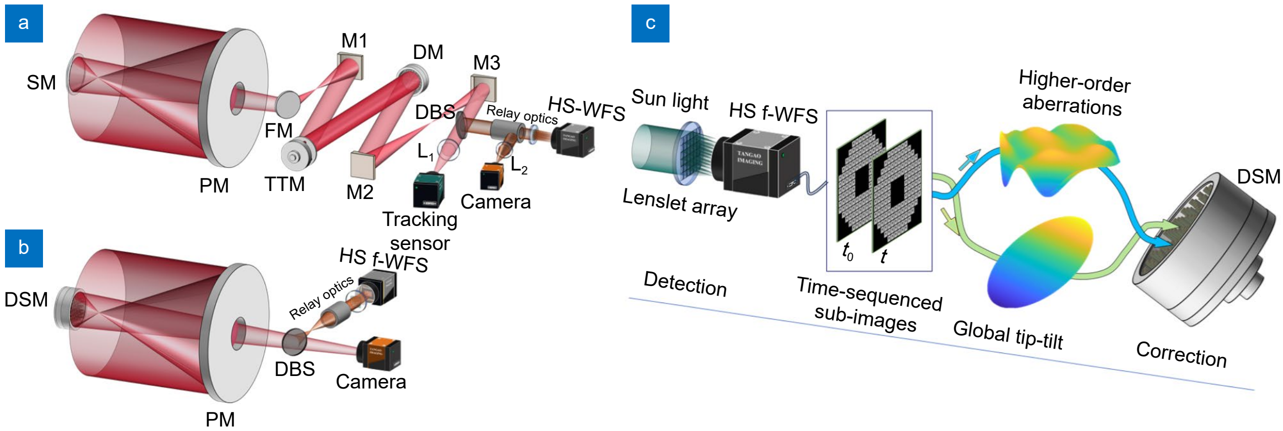

Fig. 1 | Schematic of solar telescope and ESAOT wavefront correction. (**a**) Traditional solar telescope and solar adaptive optical system. (**b**) ESAOT architecture. (**c**) Wavefront correction principle in a ESAOT. PM: Primary mirror; DSM: Deformable secondary mirror; FM: Fold mirror; TTM: Tip-tilt mirror; DBS: Dichroic beam-splitter; M1, M2, M3: collimator and off-axis parabolic mirrors for beam shrinking.

wavefront controller, which dynamically commands the deformable secondary mirror (DSM) to generate a conjugate phase profile, effectively compensating for the detected distortions. This closed-loop correction process restores the wavefront to near-flat phase distribution, achieving diffraction-limited imaging performance. While conventional cross-correlation-based HS WFS utilizes normalized cross-correlation (NCC) algorithms to enable real-time detection of higher-order aberrations in solar extended targets, it inherently fails to resolve global tip-tilt errors. This limitation stems from the NCC algorithm's exclusive focus on calculating relative sub-aperture displacement vectors relative to a reference sub-aperture, thereby discarding absolute tip-tilt information. To address this deficiency, traditional solar adaptive optics systems necessitate an auxiliary tracking sensor dedicated to global tip-tilt measurement, as illustrated in Fig. 1(a). The ESAOT architecture eliminates this requirement through an innovative paradigm: the HS f-WFS directly extracts both global tip-tilt and higher-order aberrations by analyzing temporal sequences of sub-aperture image arrays, as depicted in Fig. 1(b). Concurrently, the DSM leverages its high-stroke actuators and the inherent brightness of the solar beacon to correct tracking errors in real time, as demonstrated in the right panel of Fig. 1(c).

Furthermore, taking a 600 mm aperture ESAOT as an example, the design scheme and performance analysis are presented in Figs. S1, S2, S3, and S4.

HS f-WFS method

In solar adaptive optics systems, the Hartmann-shack wavefront sensor (HS WFS) utilizes solar photospheric structure as its natural beacon - an extended light source spanning hundreds of sub-apertures. This extend nature presents unique challenges compared to point-source systems: while point sources enable absolute tip-tilt (TT) measurement through centroid algorithms with an absolute reference position[53,54], solar observations must rely on cross-correlation techniques that compute relative sub-aperture displacements, inherently obscuring global TT information[55–57]. This fundamental difference necessitates specialized correlation-based analysis methods for solar applications. The HS WFS methodology for extended targets introduces a normalized cross-correlation (NCC) framework where a reference sub-image $I_{\text{ref}}(u, v)$ is strategically selected from the microlens array (MLA). Subsequent sub-images are then analyzed through computational cross-correlation coefficient (CCC) mapping, mathematically expressed for the (i^{th}, j^{th}) microlens as[58]:

$$NCC_{i,j}(x,y) = \frac{\int_{S_r} I_{\text{ref}}(u,v) I_{i,j}(u+x, v+y) \mathrm{d}u\mathrm{d}v}{\sqrt{\int_{S_r} I_{\text{ref}}^2(u,v)\mathrm{d}u\mathrm{d}v}\sqrt{\int_{S_r} I_{i,j}^2(u,v)\mathrm{d}u\mathrm{d}v}}\,, \tag{1}$$

where $I_{i,j}(u, v)$ represents the intensity distribution of the sub-image corresponding to the (i, j)th microlens of the microlens array (MLA); (u, v) denotes the coordinate position of the sub-image in the horizontal and vertical directions, respectively; (x, y) indicates the offsets between the reference sub-image and the calculated sub-image in the horizontal and vertical directions, respectively; S_r is the effective area of the normalized cross-correlation (NCC) coefficient distribution.

The calculated coefficient distribution of $NCC_{i,j}(x, y)$ represents the offset of the sub-image relative to the reference micro-lenslet in both the horizontal and vertical directions for the micro-lenslet located at row i and column j. By applying the centroid algorithm, the corresponding slopes in the horizontal and vertical directions can be derived, as shown in the following expressions:

$$\begin{aligned} g_x(i,j) &= \frac{\int_{S_r} x \times NCC_{i,j}(x,y)\mathrm{d}x\mathrm{d}y}{\int_{S_r} NCC_{i,j}(x,y)\mathrm{d}x\mathrm{d}y} \times \frac{1}{f} \\ g_y(i,j) &= \frac{\int_{S_r} y \times NCC_{i,j}(x,y)\mathrm{d}x\mathrm{d}y}{\int_{S_r} NCC_{i,j}(x,y)\mathrm{d}x\mathrm{d}y} \times \frac{1}{f} \end{aligned} , \tag{2}$$

where f presents the focal length of micro-lenslets of HS WFS.

The slope distribution of the overall pupil of the HS WFS can be detected using Eq. (2), and wavefront aberration information can subsequently be obtained through a wavefront reconstruction algorithm, as illustrated in Fig. 2. However, traditional methods that rely on the NCC algorithm typically fail to capture global tip-tilt information. This is because they only compute the relative position offsets and slopes of each sub-aperture with respect to a reference sub-aperture.

Drawing on existing research, we introduce an innovative method and algorithm for measuring full-wavefront aberrations using a single Hartmann-shack full-wavefront sensor (HS f-WFS). This method enables the simultaneous detection of both global tip-tilt and higher-order aberrations, addressing a key limitation of conventional approaches. Figure 3 illustrates the measurement principle of the proposed HS f-WFS, which leveraging time sequences of sub-image arrays to obtain global tip-tilt and high-order aberration information. Unlike conventional fine-tracking sensors that rely on a single, fixed reference image, the proposed method utilizes the sub-image array of the HS f-WFS as the reference for global tip-tilt measurement. At the same time, after calibrating the higher-order aberrations at the starting moment using its own sub-images, the higher-order wavefront aberration information can be similarly obtained from these sequential sub-aperture images. A sunspot, with their high intrinsic contrast (~10% intensity variation), are prioritized as wavefront sensing beacons due to superior signal-to-noise ratios in correlation algorithms. However, as mentioned above, large sunspots occupying central

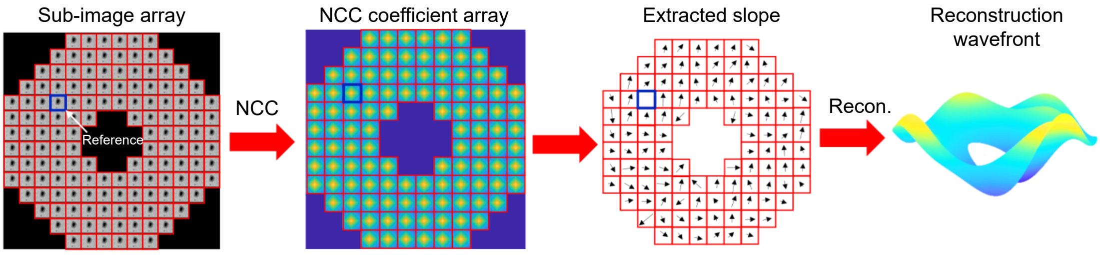

Fig. 2 | Wavefront detection process of conventional cross-correlation HS WFS. NCC: Normalized cross-correlation; Recon.: Reconstruction.

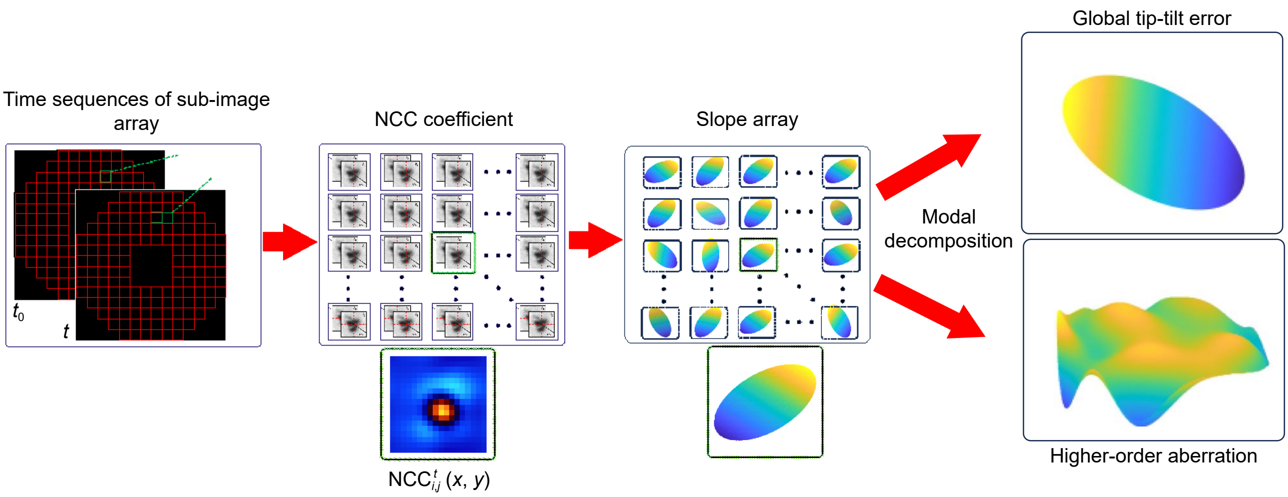

Fig. 3 | Measurement principle of the HS f-WFS for detecting global tip-tilt and higher-order aberrations using time-sequenced sub-images.

sub-aperture FoV regions can reduce sensitivity to sub-pixel shifts. To mitigate this, small sunspots can be used or the steep intensity gradients at the penumbral edges of sunspots can be exploited to maintain shift sensitivity. While solar granulation is a potential lighthouse, its low contrast (<2%) complicates closed-loop stability in strong turbulence.

Specifically, the reference sub-image array is captured at time t_0, and the intensity distribution of the sub-images corresponding to the i^{th} row and j^{th} column of the sub-aperture is denoted as $I^{t_0}_{i,j}(u, v)$, where (u, v) represents the positional coordinates of the sub-image in the horizontal and vertical directions. At another time t, the intensity distribution of the sub-images detected by the HS WFS is denoted as $I^t{}_{i,j}(u, v)$. By applying the NCC algorithm, similar to Eq. (1), the cross-correlation factor between the corresponding sub-images at times t and t_0 can be calculated as follows:

$$NCC^t_{i,j}(x,y) = \frac{\int_{S_r} I^{t_0}_{i,j}(u,v) I^t_{i,j}(u+x, v+y) \mathrm{d}u\mathrm{d}v}{\sqrt{\int_{S_r} \left[I^{t_0}_{i,j}(u,v)\right]^2 \mathrm{d}u\mathrm{d}v} \sqrt{\int_{S_r} \left[I^t_{i,j}(u,v)\right]^2 \mathrm{d}u\mathrm{d}v}}, \tag{3}$$

where $I^{t_0}_{i,j}(u, v)$ denotes the intensity distribution of the sub-image in the i^{th} row and j^{th} column HS f-WFS at the reference time t_0, and $I^t{}_{i,j}(u, v)$ represents the intensity distribution of the sub-image in the same position at time t.

By employing the centroid algorithm, the proposed HS f-WFS achieves precise determination of the position offset and corresponding slope for all sub-images as they evolve from the reference time t_0 to the current time t. A pivotal innovation of this method is the introduction of time-sequenced reference sub-images to measure global tip-tilt errors. Unlike conventional techniques, which compute the relative slope between each sub-image at the current moment and a static reference position, our approach calculates the relative slope between each sub-image at the current moment t and its corresponding sub-image at the reference moment t_0. This novel strategy enables the synchronous detection of global tip-tilt errors and higher-order wavefront aberrations using only a single sub-image array obtained from the cross-correlation HS f-WFS. Consequently, the overall position offset and slope of a sub-image are calculated relative to the sub-image at the reference time t_0, as detailed in the following equation:

$$\begin{aligned} g^t_x(i,j) &= \frac{\int_D x \times NCC^t_{\text{tip-tilt},(i,j)}(x,y)\mathrm{d}x\mathrm{d}y}{\int_D NCC^t_{\text{tip-tilt},(i,j)}(x,y)\mathrm{d}x\mathrm{d}y} \times \frac{1}{f} \\ g^t_y(i,j) &= \frac{\int_D y \times NCC^t_{\text{tip-tilt},(i,j)}(x,y)\mathrm{d}x\mathrm{d}y}{\int_D NCC^t_{\text{tip-tilt},(i,j)}(x,y)\mathrm{d}x\mathrm{d}y} \times \frac{1}{f} \end{aligned}, \tag{4}$$

where f is the focal length of each micro-lenslet of HS f-WFS.

Equation (4) captures the local slope distribution associated with temporal changes in wavefront aberration between between the reference moment t_0 and the current moment t. This distribution inherently incorporates both global tip-tilt errors and higher-order wavefront aberrations. By reconstructing the local slope information derived from Equation (4)—using zonal [59], modal[60], or deep-learning-based[61] methods—the corresponding temporal variation in wavefront aberration can be determined. This aberration change, denoted as $\Phi_{t-t_0}(x, y)$, can be mathematically expressed as:

$$\begin{aligned} \Phi_{t\text{-}t_0}(x,y) &= \text{recon.}\{g^t_x(i,j), g^t_y(i,j)\} \\ \Phi_t(x,y) &= \Phi_{t\text{-}t_0}(x,y) + \Phi_{t_0}(x,y) \end{aligned}, \tag{5}$$

where recon.{} denotes wavefront reconstruction process, while $\Phi_t(x, y)$ and $\Phi_{t_0}(x, y)$ represent the actual wavefront aberrations at the moment t and the reference moment t_0, respectively.

Notably, the reference wavefront aberration $\Phi_{t_0}(x, y)$ must first be detected and reconstructed via conventional wavefront sensing methods, as demonstrated in Eq. (2) and Fig. 2. However, due to inherent limitations of such methods, $\Phi_{t_0}(x, y)$ inherently excludes global tip-tilt information. In contrast, the wavefront phase change $\Phi_{t\text{-}t_0}(x, y)$, calculated as the difference between the current moment t and the reference t_0, encapsulates both higher-order wavefront aberrations and the global tip-tilt error introduced during the temporal evolution. By integrating the statically measured reference wavefront $\Phi_{t_0}(x, y)$ with the dynamically detected phase change $\Phi_{t\text{-}t_0}(x, y)$, one can simultaneously derive the absolute higher-order aberration and the relative global tip-tilt error at moment t, thereby enabling comprehensive and precise reconstruction of the full wavefront aberration profile.

The detected wavefront aberrations can ultimately be decomposed into Zernike polynomials via modal decomposition. In this framework, the first two non-piston terms (Z_1 and Z_2) correspond to global tip-tilt errors, while subsequent terms represent higher-order aberrations, as expressed by:

$$\begin{aligned}\Phi_t(x,y) &= \sum_{k=0}^{N} a_k Z_k(x,y) \\ &= a_0 Z_0(x,y) + \sum_{k=1}^{2} a_k Z_k(x,y) + \sum_{k=3}^{N} a_k Z_k(x,y) \\ &= \Phi_{\text{piston}}(x,y) + \Phi_{\text{tip-tilt}}(x,y) + \Phi_{\text{high-order}}(x,y)\ ,\end{aligned} \tag{6}$$

where $Z_k(x, y)$ and a_k denote the k^{th} order Zernike polynomial and its corresponding coefficient, respectively. Φ_{piston}, $\Phi_{\text{tip-tilt}}$ and $\Phi_{\text{higher-order}}$ represent the piston term, global tip-tilt error, and higher-order aberrations, respectively.

Atmospheric phase screen simulations based on Kolmogorov spectral analysis reveal that wavefront aberrations induced by atmospheric turbulence exhibit spatiotemporal randomness. Notably, global tip-tilt constitutes the dominant component of atmospheric aberrations, yet its temporal frequency is significantly lower than that of higher-order atmospheric aberrations[62]. Consequently, the deformable secondary mirror (DSM) can employ distinct control bandwidths for global tip-tilt and higher-order aberration compensation, despite the Hartmann-shack full-wavefront sensor (HS f-WFS) providing higher-frequency wavefront sampling for both global tip-tilt and higher-order aberrations. Besides, HS f-WFS matches the computational efficiency of traditional methods updating references dynamically avoids added processing time. This innovation resolves tip-tilt loss in extended-target sensing while ensuring real-time performance.

Results and discussion

Optimizing design results

The actuator configuration of the DSM and the spatial resolution of the HS f-WFS are critical parameters governing the stability of wavefront correction in the ESAOT system. In this study, we have optimized the design of the HS f-WFS resolution and the actuator position of the DSM, based on the 600 mm ESAOT prototype. The specific design scheme and detailed parameters are presented in Fig. S1 and Tables S1, S2, respectively. Figure 4(a) illustrates the preliminary DSM actuator layout, featuring 61 actuators uniformly distributed across a Φ=590 mm aperture (matching the primary mirror diameter), with an actuator spacing of approximately 72.9 mm. However, it is evident that seven actuators positioned within the central sheltered region are non-functional due to physical obstruction. To address this limitation, we have optimized the actuator layout by repositioning the central actuators to the edge of the obscuration zone, as depicted in Fig. 4(b), ensuring full utilization of the optically active area. This refined design achieves a uniform actuator distribution with a reduced spacing of approximately 62.8 mm, out performing the Greenwood standard[63] estimate of 66.4 mm. The 61-DSM features a clear aperture of Φ=174 mm with a central obscuration ratio of 35.6% (total diameter Φ=210 mm including protective structures). Each actuator provides ±3 μm stroke with inter-actuator coupling below 10%, enabling precise surface shaping for wavefront correction. Practical characterization of the actuator influence functions will be conducted through dual-modal measurements: offline interferometric profiling and online HS f-WFS calibration.

To quantify the correction capability of the 61-actuator deformable secondary mirror (61-DSM), we evaluate its performance in fitting and compensating the first 25 orders of Zernike polynomials. The residual RMS error, expressed as a percentage of the original aberration RMS, serves as the metric for assessing the 61-DSM's wavefront fitting capability. As summarized in Fig. 4(c), both the preliminary uniform layout and optimized actuator configuration demonstrate comparable correction performance for the first 5 Zernike modes, with the initial design marginally outperforming the optimized version. For higher-order Zernike modes, the optimized layout achieves a significant improvement, reducing the average residual error by 4.33% compared to the preliminary design.

The resolution of the HS f-WFS has been optimized using a direct wavefront gradient algorithm, with the objective of minimizing the condition number (CN) of the control matrix. As demonstrated in Fig. 4(d), we performed comprehensive comparative analyses of condition number (CN) variations across different sensor resolutions. Comparative analysis reveals that as the HS WFS resolution increases, the condition number of the control matrix for the ESAOT system decreases. However, while the condition number stabilizes for resolutions beyond 12×12, a notable performance drop occurs at 13×13, primarily due to aliasing effects caused by insufficient spatial sampling density of the DSM actuators. This resolution-dependent saturation phenomenon guided

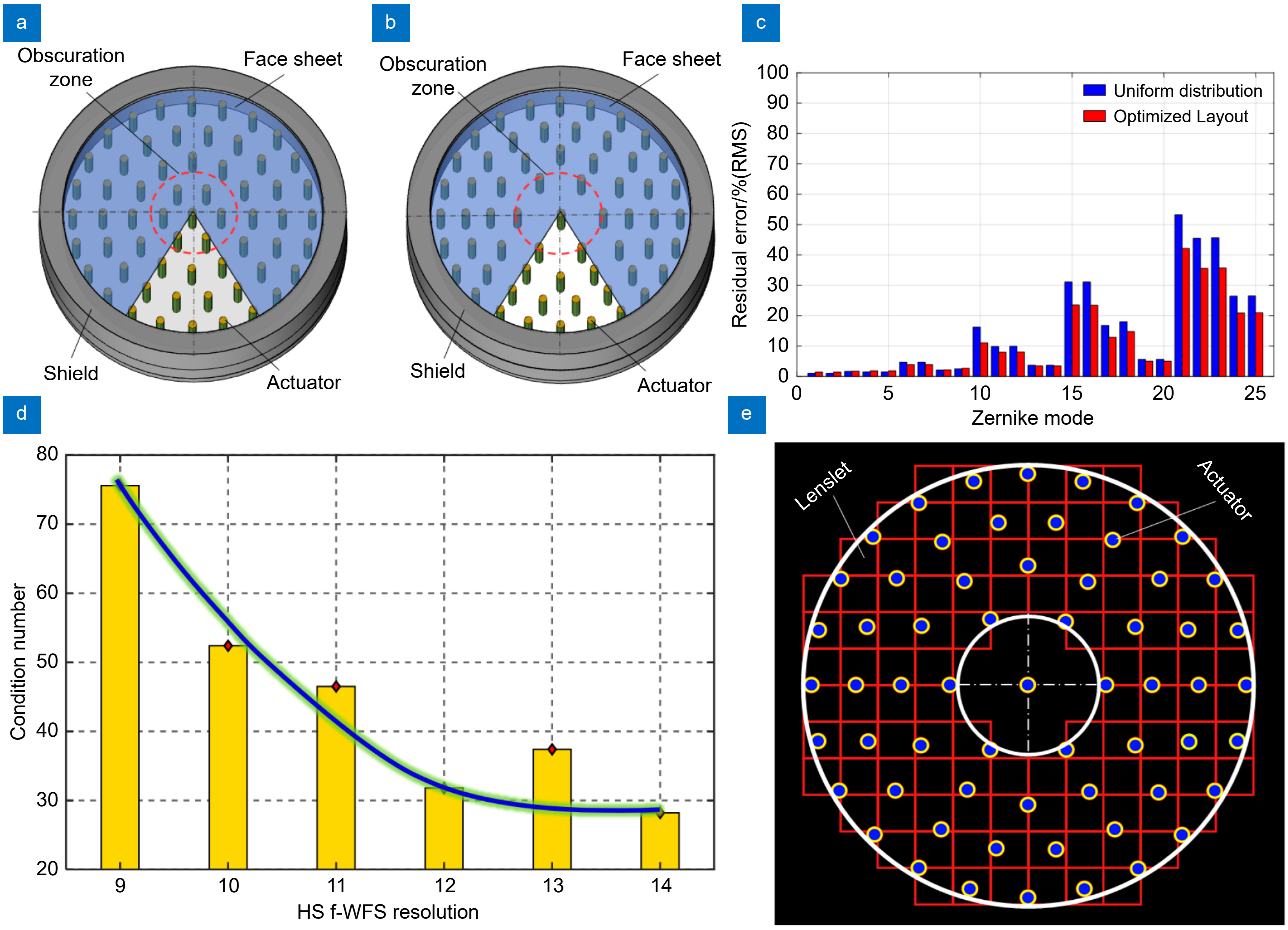

Fig. 4 | Design Optimization of the 61-DSM and the HS f-WFS configuration. (**a**) Preliminary actuator distribution of the 61-DSM. (**b**) Optimized actuator arrangement of the 61-DSM. (**c**) Zernike mode compensation performance (the first 25 orders) for both actuator configurations. (**d**) Control matrix condition number versus HS f-WFS spatial sampling resolution. (**e**) Co-registered HS f-WFS lenslet array and DSM actuator positions. Annotation: Annular region bounded by white circles denotes the clear aperture.

our final selection of 12×12 configuration, achieving optimal balance between computational efficiency and measurement accuracy. The implemented design features 96 active sub-apertures within the light-through aperture. Figure 4(e) illustrates the optimized geometric configuration, showing precise alignment between the HS f-WFS sub-apertures and the DSM actuators. The HS f-WFS is designed to have a field of view of about 24" × 24", and each sub-aperture can acquire solar atmosphere images of the corresponding field of view, and the actual effective corrected field of view is related to the isoplanatic region (generally about 10" – 20"), which is much smaller than the corresponding corrected field of view of the MCAO (generally about 1' or larger). To achieve wider-field correction, we employ a combined approach of proposed SAO and image post-processing technique —a practical solution that balances performance and system complexity.

Numeric simulation

To validate the performance of the ESAOT system, we conducted numerical simulations of wavefront correction using random phase screens that adhere to the Kolmogorov turbulence model. The simulations were based on a 600 mm ESAOT prototype, with design schemes and detailed parameters presented in Fig. S1, and Tables S1, S2. External site conditions were incorporated to ensure the simulations accurately reflected realistic atmosphere turbulence scenarios. As illustrated in Fig. S2, the median atmospheric coherence length (r_0) measured at the TiO band was approximately 6.07 cm, yielding a ratio of D/r_0≈9.7. By applying the Kolmogorov turbulence model, we simulated and analyzed wavefront aberrations and their temporal evolution for solar photospheric images, comparing the results before and after correction with the 61-DSM.

The detailed simulation process, outlined in Fig. 5,

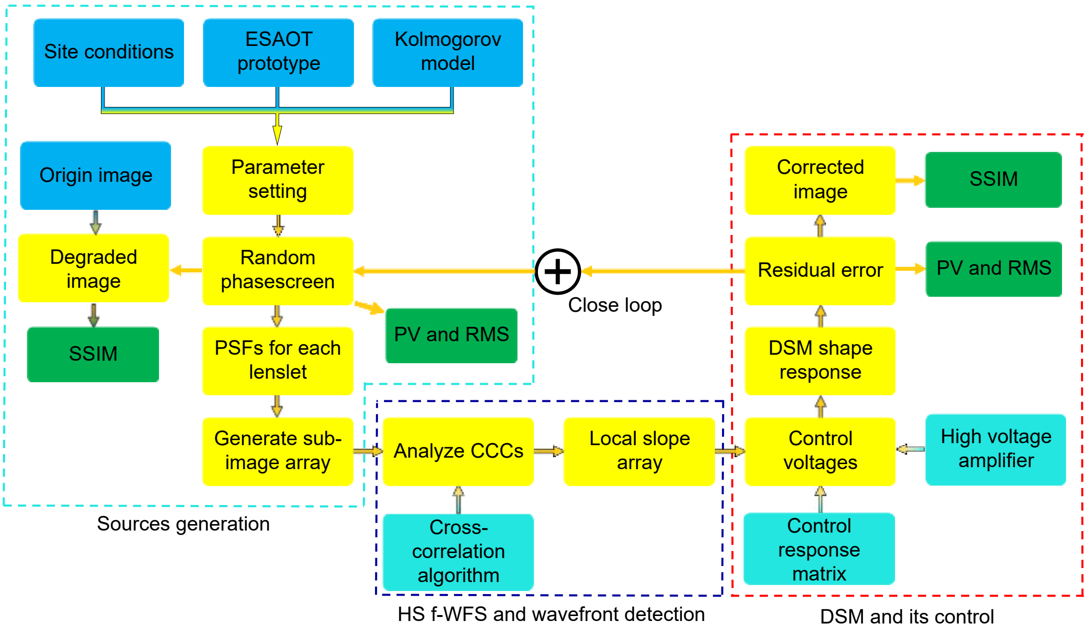

Fig. 5 | Schematic diagram of the numerical simulation workflow (CCC: Cross-correlation coefficient).

began with the generation of a series of random phase screens based on site-specific atmospheric conditions and the 600 mm ESAOT prototype parameters. Degraded images were then produced by convolving the original image with the corresponding point spread function (PSF). Wavefront aberrations were quantified using peak-to-valley (PV) and root mean square (RMS) values, while image quality was assessed using the structural similarity index (SSIM)[64]. For each lenslet in the HS f-WFS, the PSF was estimated from optical parameters and local phase distributions, and sub-image arrays were generated for every phase screen frame. Using a cross-correlation algorithm, we calculated the cross-correlation coefficient (CCC) for each lenslet, determining the position offsets and local slopes relative to a reference sub-image at the reference moment. This process simulated the HS f-WFS wavefront detection, enabling the extraction of global tip-tilt and higher-order Zernike polynomial components. Control voltages for the 61-DSM were then computed based on the system's control matrix, derived from the influence functions of each actuator. The control matrix is generated through a direct slope algorithm: actuator influence functions measured by the wavefront sensor form the interaction matrix, while wavefront aberration slopes serve as input targets, with actuator voltages optimally computed via singular value decomposition (SVD) and matrix operation. These voltages drove the DSM to partially correct the detected global tip-tilt and higher-order aberrations, though residual wavefront errors remained after correction. To emulate closed-loop operation, we generated 1,600 frames of dynamically evolving phase screens, simulating continuous atmospheric turbulence. The residual wavefront error from each frame was added to the subsequent phase screen as an initial aberration, forming a closed-loop correction process. This iterative approach allowed us to evaluate the ESAOT system's performance under realistic, time-varying turbulence conditions.

Figure 6(a) and 6(b) depict a random phase screen and its corresponding first 65 Zernike mode coefficients. The generated phase screen exhibits a PV value of 2.89λ and an RMS value of 0.48λ, where λ represents the imaging wavelength. Despite the broad spatial frequency distribution of the phase screen, low-order wavefront aberrations constitute the dominant component. Statistical analysis of 1,600 random phase screens indicates that the first 65 Zernike modes account for 96.20% of the total RMS, while the first 25 modes contribute 93.14%.

Closed-loop correction was validated using 1,600 frames of dynamic random phase screens. Figure 6(c, d) show the temporal evolution of wavefront RMS and image SSIM before and after correction. Results demonstrate a 69.9% reduction in average wavefront RMS (from 0.3715λ to 0.1130λ) and a 125% improvement in average SSIM (from 0.2814 to 0.6332). These metrics confirm the 600 mm ESAOT's exceptional ability to correct atmospheric turbulence-induced aberrations, achieving near-diffraction-limited imaging while significantly enhancing

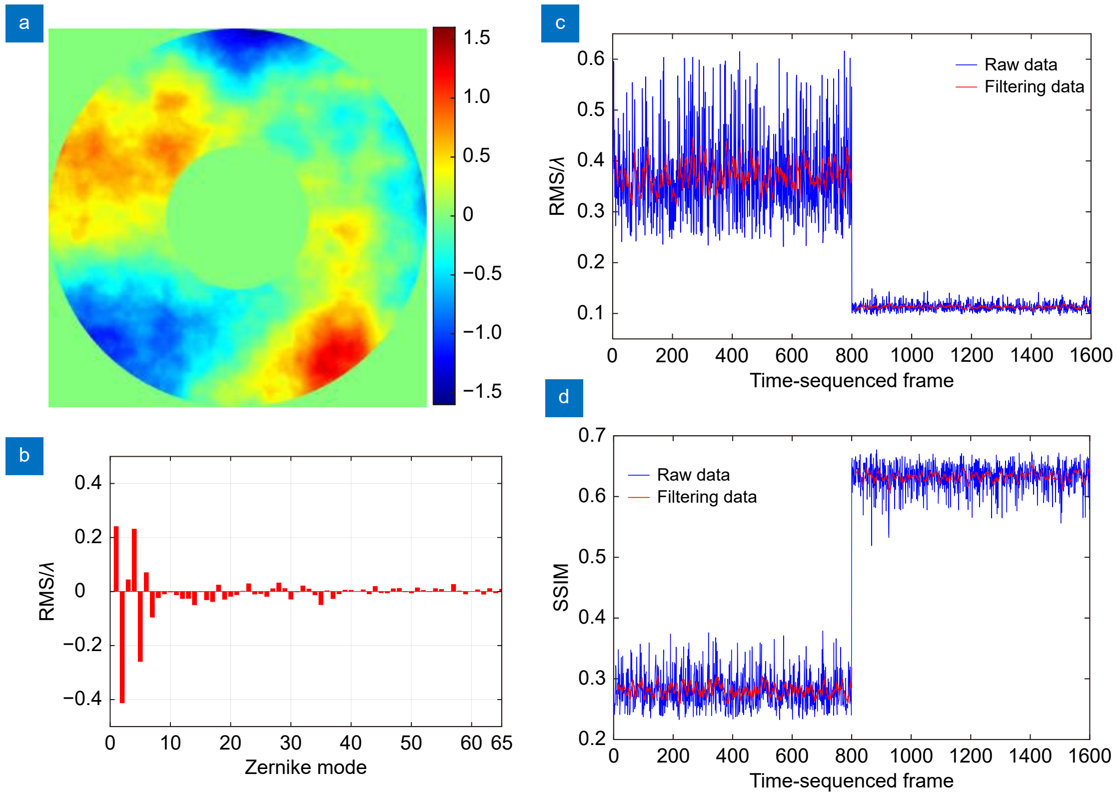

Fig. 6 | Numerical validation process and outcomes. (**a**) Representative random phase screen generated under Kolmogorov turbulence conditions. (**b**) First 65 Zernike mode coefficients corresponding to the phase screen in (a). (**c**) Temporal evolution of wavefront aberration RMS values before and after 61-DSM correction. (**d**) Structural similarity index (SSIM) progression for degraded and corrected images, reflecting quality improvement through adaptive optics compensation.

image quality. This capability enables the identification of subtle solar activity features, as illustrated by the comparative images (original, diffraction-limited, and corrected) in Fig. S5.

Laboratory validation

To further verify the feasibility of the proposed ESAOT method, we conducted laboratory experiments using a 61-actuator DSM integrated with PZT actuators, face sheet and supporting structure, as shown in Fig. 7(a) and 7(b). The DSM was polished using magnetorheological jet polishing, coated with a silver layer protected by SiO_2, and prepared for testing (Fig. 7(b, c)). Closed-loop adaptive optics testing demonstrated exceptional surface accuracy, achieving 12.5 nm RMS (λ/56.5 at TiO band wavelength), as confirmed by phase-shifting interferometry (Fig. 7(d)).

An indoor experimental system was established to evaluate the ESAOT's wavefront correction capability (Fig. 7(e)). Leveraging the DSM's concave ellipsoid geometry, which creates dual focal points (F1, F2), we positioned a light source at F1 to simulate point/extended objects. Light reflected from the DSM was re-imaged at F2, then collimated by lens L1 and split by a beam splitter (BS). The reflected beam passed through imaging optics to lens L4's focal plane and a photodetector camera, enabling real-time monitoring of image quality before and after correction. The transmitted beam was relayed by lenses L2–L3 to match the HS f-WFS aperture for wavefront aberration detection, with a field stop limiting its field of view. Dynamic turbulence was simulated using a heater-generated random phase screen, while a custom hexapod mechanism[65] enabled precise DSM attitude adjustment. For closed-loop control, we utilizes a proportional-integral (PI) architecture whose parameters are systematically tuned through optimizing both the control bandwidth and the overshoot of the control error. Under the constraint that the control error overshoot does not exceed 5 dB, we increase the control bandwidth of the system by incrementally increasing the parameters. The real-time controller operates on a Windows platform with real-time performance ensured by thread and process prioritization and CPU affinity optimizations. Experimental results demonstrated significant

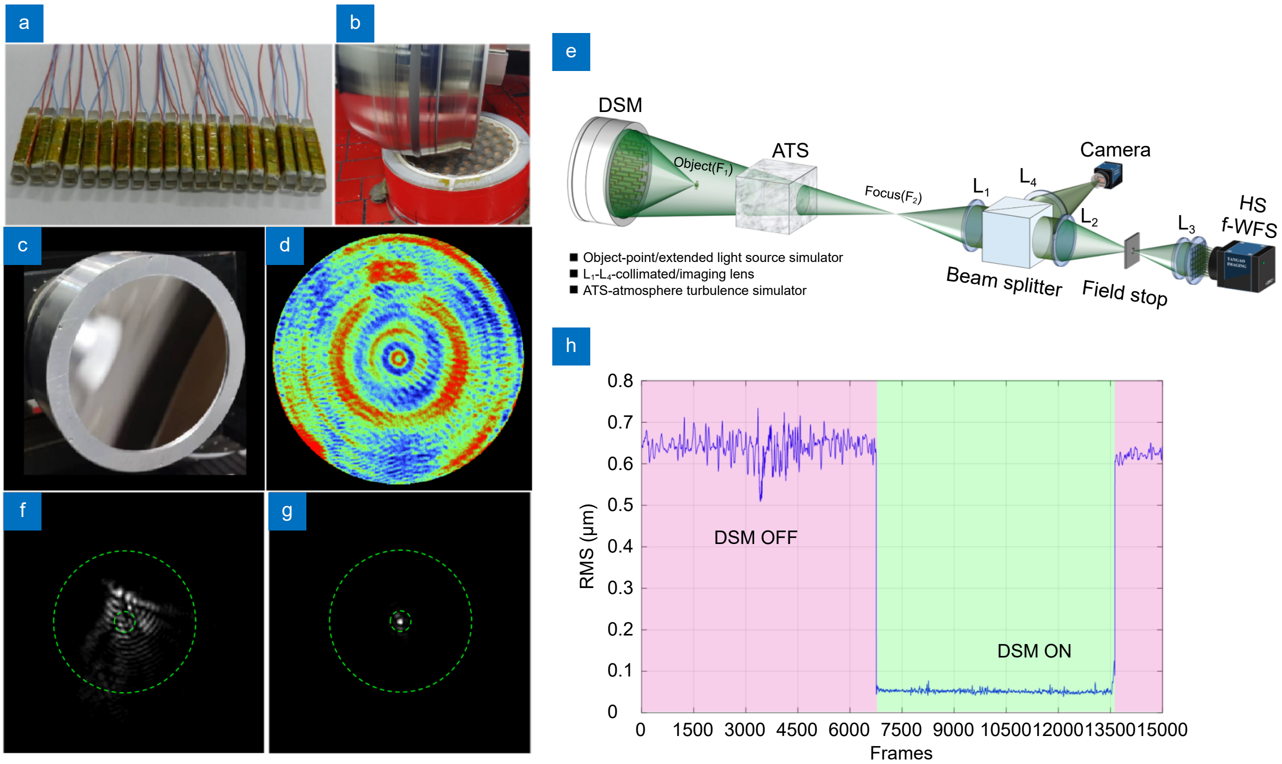

Fig. 7 | Laboratory validation of ESAOT using the 61-actuator DSM. (**a**) Screened PZT actuators. (**b**) Optical polishing of the 61-DSM. (**c**) Delivered 61-DSM. (**d**) Surface profile of the 61-DSM after self-correction (*RMS*=12.5 nm). (**e**) Schematic of laboratory validation system. (**f**) Image before wavefront correction. (**g**) Image after wavefront correction, showing a 15-fold increase in peak intensity. (**h**) Dynamic wavefront aberration correction results: the purple region represents the RMS curve with the DSM OFF (average *RMS*≈0.91λ), and the green region represents the RMS curve with the DSM ON (average *RMS*≈0.07λ).

performance improvements: wavefront aberrations before and after correction are shown in Fig. S6, while Figs. 7(f), 7(g) and S7 illustrate enhanced image quality for both point and extended objects. Notably, the point object's peak intensity increased over 15-fold post-correction, confirming the system's exceptional wavefront correction capability.

The experimental system successfully corrected simulated dynamic wavefront aberrations, with the HS f-WFS operating at 1,600 fps and the DSM control system achieving >50 Hz bandwidth. As shown in Fig. 7(h), the RMS of wavefront aberration decreased from 0.51–0.73 μm (avg. 0.64 μm, 0.91λ) to 0.043–0.078 μm (avg. 0.05 μm, 0.07λ) after DSM correction—a reduction exceeding one order of magnitude. These results demonstrate the system's robust capability for dynamic wavefront correction.

First light on-sky observation

A 600 mm aperture ESAOT prototype was successfully developed and integrated at Lijiang Observation Station, a premier astronomical site known for its exceptional atmospheric conditions. The system, comprising optical, structural, and control components, was fully assembled by January 2023. Figure 8(a–c) illustrates the main optical components of the 600 mm ESAOT prototype, highlighting its advanced design and integration. Key optical elements include:

- **Primary mirror (PM):** fabricated from ultra-low expansion (ULE) material in a lightweight honeycomb structure, the PM was precision-polished using magnetorheological jet polishing, achieving an RMS surface error of 8 nm over a 590 mm clear aperture.
- **Deformable secondary mirror (DSM):** a 61-actuator DSM integrated with a hexapod structure for precise alignment during system integration and on-sky observations.
- **Fold mirror (FM):** constructed from silicon carbide (SiC) material, the FM was polished and coated to ensure high reflectivity and thermal stability.
- **Heat-stop:** a custom-designed component to limit the field of view (FoV) and mitigate internal thermal

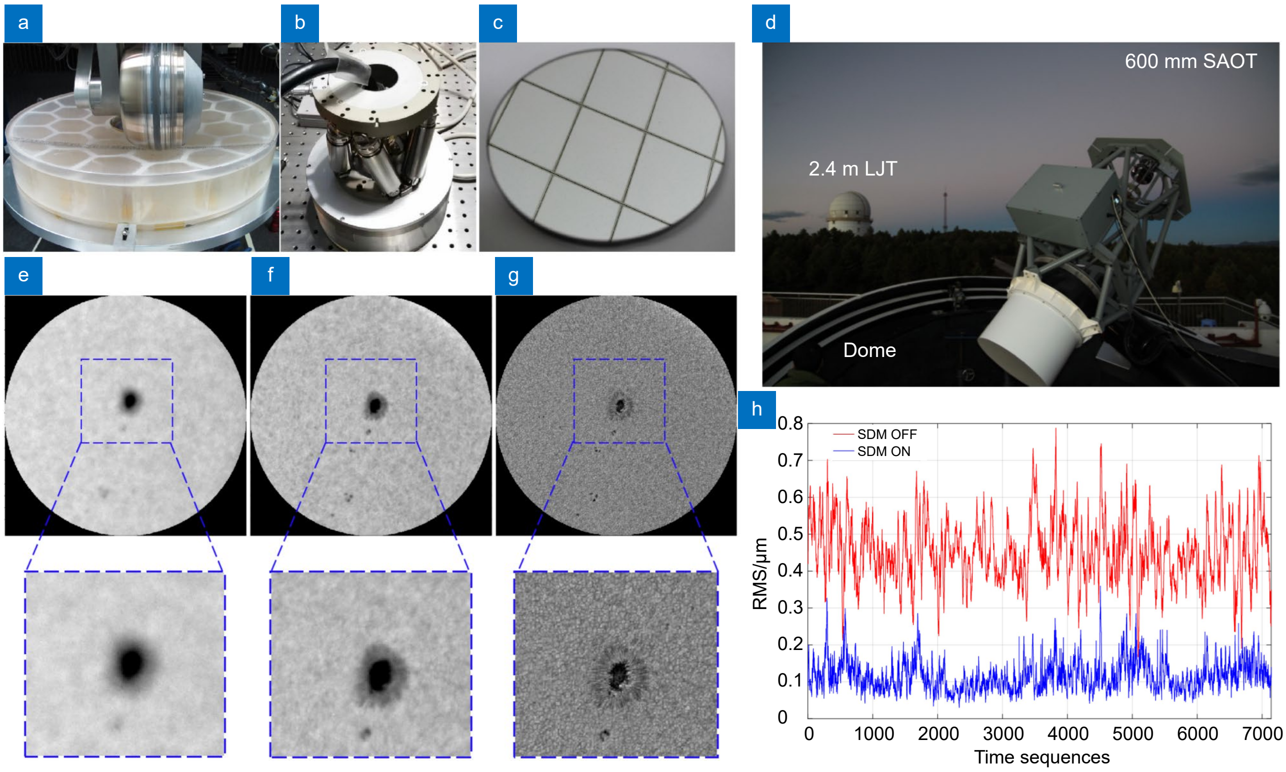

Fig. 8 | Prototype of the 600 mm ESAOT and its first-light on-sky observation results. (**a**) Light-weighted primary mirror (PM) during polishing. (**b**) DSM integrated with the hexapod structure. (**c**) Completed fold mirror (FM). (**d**) Operational 600 mm ESAOT, with the 2.4 m Lijiang telescope visible approximately 300 m away. First-light images of the 600 mm ESAOT capturing the solar photosphere. (**e**) Uncorrected image. (**f**) Image after wavefront correction. (**g**) Image after wavefront correction and reconstruction. (**h**) Time-varying RMS of high-order wavefront aberrations before (average RMS≈0.71λ) and (average RMS≈0.17λ) DSM correction.

effects through active cooling.

The 600-mm ESAOT prototype was mounted on the roof of a two-story building, with its base situated approximately 10 meters above ground level. To safeguard the telescope from adverse environmental conditions such as severe wind vibrations and precipitation (rain and snow), a protective hemispherical dome with a diameter of 6 meters was installed. Following the extended rainy season at the Lijiang Observation Station, the 600-mm ESAOT successfully underwent integration testing in September 2023 and commenced its observational operations, as depicted in Fig. 8(d). On September 15, 2023, the telescope captured its first light from the solar atmosphere, specifically from the photosphere. Figure 8(e–g) presents a comparative analysis of images captured with and without the DSM in operation, along with the images post-DSM correction and speckle reconstruction, which derives target amplitude/phase through the multi-frame statistical analysis in Fourier domain-a standard methodology for solar image post-reconstruction[64]. After SAO correction and reconstruction processing, the resolution of solar atmospheric imaging is increased step by step. In comparison, ESAOT addresses this by real-time correction of both turbulence-driven phase aberrations. This enhances image SNR, providing high-quality input data for reconstruction while ensuring system effectiveness and algorithmic precision. While ESAOT effectively mitigate atmospheric distortions, fundamental limitations persist including residual wavefront errors and anisoplanatic effects. These effects produce corrected images with inherently low contrast. However, AO-preprocessed images provide an essential precursor for post-processing, enabling final contrast enhancements. These images cover a field of view of approximately "117×117". The tracking errors before and after DSM correction are illustrated in Fig. S8.

The DSM's capability to correct dynamic high-order wavefront aberrations is particularly noteworthy. As illustrated in Fig. 8(h), prior to DSM correction, the RMS value of dynamic wavefront aberrations (excluding global tip-tilt errors) fluctuated between 0.3 μm and 0.6 μm, corresponding to approximately 0.43λ to 0.85λ. The average RMS value of these aberrations was 0.5 μm, or about 0.71λ. Post-DSM correction, the RMS values were significantly reduced, ranging from 0.05 μm to 0.18 μm, with an average of 0.12 μm, equivalent to approximately 0.071λ to 0.26λ and 0.17λ, respectively. This represents an approximate 83% reduction in high-order wavefront aberrations, markedly enhancing the imaging quality of the solar atmospheric photosphere and providing superior image data for subsequent speckle reconstruction processes. However, due to dynamic environmental perturbations (e.g., atmospheric turbulence, wind-induced vibrations) and limitations in the real-time controller (RTC) bandwidth, the tracking accuracy and high-order wavefront aberration correction capabilities are weaker than those in controlled indoor environments and remain sub-optimal. The primary limitation stems from TCP/IP induced network latency in high-voltage amplifier (HVA) communication, which fundamentally limits bandwidth scalability improvement. Future efforts will prioritize hardware upgrades and adaptive algorithm optimization to mitigate these challenges and enhanced wavefront correction performance.

Conclusions

In this study, we propose a novel ESAOT architecture that integrates a solar adaptive optics system into conventional solar telescope frameworks. A groundbreaking methodology is introduced for synchronous full-wavefront measurement, encompassing both global tip-tilt and high-order aberrations, utilizing a single cross-correlation HS f-WFS.

The detected aberrations are subsequently corrected via a uniquely designed concave ellipsoidal DSM. This integrated approach significantly enhances system compactness, optical transmission efficiency, and operational reliability, while simultaneously mitigating instrumental polarization effects. Remarkably, the ESAOT achieves comprehensive fast steering and wavefront correction capabilities without introducing structural complexity beyond that of standard solar telescopes.

To validate this concept, a 600-mm ESAOT prototype was developed and rigorously evaluated through numerical simulations and laboratory experiments employing a 61-actuator DSM testbed. Field implementation at the Lijiang Observation Station successfully demonstrated first-light observations of the solar photosphere. Quantitative analyses revealed substantial performance enhancements: post-DSM correction yielded a minimum 5.3-fold improvement in tracking accuracy and a 4.17-fold reduction in wavefront aberration RMS values. These empirical results conclusively verify the effectiveness and practical applicability of the proposed ESAOT paradigm.

As the inaugural implementation of its kind, this work establishes a critical reference framework for advancing current and next-generation large-aperture solar telescope designs. While the prototype demonstrates promising capabilities, performance optimization remains achievable through four key future developments: (1) Acceleration of wavefront processor computational throughput; 2) Enhancement of HS f-WFS frame-rate resolution; 3) Refinement of hexapod-driven low-order aberration compensation; 4) Developing advanced methodologies for low-contrast solar AO, specifically targeting wavefront sensing and correction using extremely low-contrast features as guidemarks. These targeted improvements will facilitate near-diffraction-limited imaging performance, thereby unlocking unprecedented observational precision for solar atmospheric studies.

References

1. Rimmele T, Keil S, Dooling D. Building the world's largest optical solar telescope. SPIE (2007).
2. MacTaggart D, Prior C, Raphaldini B et al. Direct evidence that twisted flux tube emergence creates solar active regions. *Nat Commun* **12**, 6621 (2021).
3. Stangalini M, Verth G, Fedun V et al. Large scale coherent magnetohydrodynamic oscillations in a sunspot. *Nat Commun* **13**, 479 (2022).
4. Yuan D, Fu LB, Cao WD et al. Transverse oscillations and an energy source in a strongly magnetized sunspot. *Nat Astron* **7**, 856–866 (2023).
5. Stangalini M. Wave energy in the solar atmosphere. *Nat Astron* **7**, 761–762 (2023).
6. Clery D. 'Campfires' may drive heating of solar atmosphere. *Science* **372**, 557–558 (2021).
7. Yan XL, Xue ZK, Jiang CW et al. Fast plasmoid-mediated reconnection in a solar flare. *Nat Commun* **13**, 640 (2022).
8. Ishikawa R, Bueno JT, Del Pino Alemán T et al. Mapping solar magnetic fields from the photosphere to the base of the corona. *Sci Adv* **7**, eabe8406 (2021).
9. Jenkins JM, Keppens R. Resolving the solar prominence/filament paradox using the magnetic Rayleigh-Taylor instability. *Nat Astron* **6**, 942–950 (2022).
10. Hotta H, Kusano K. Solar differential rotation reproduced with high-resolution simulation. *Nat Astron* **5**, 1100–1102 (2021).
11. Dong CF, Wang L, Huang YM et al. Reconnection-driven energy cascade in magnetohydrodynamic turbulence. *Sci Adv* **8**, eabn7627 (2022).
12. Boucheron LE, Vincent T, Grajeda JA et al. Solar active region magnetogram image dataset for studies of space weather. *Sci*

Data **10**, 825 (2023).
13. Wheatland MS. Real-time solar coronal modelling. *Nat Astron* **7**, 1150–1151 (2023).
14. Li KF, Tung KK. Solar cycle as a distinct line of evidence constraining earth's transient climate response. *Nat Commun* **14**, 8430 (2023).
15. von der Lühe O, Schmidt W, Soltau D et al. GREGOR: a 1.5m telescope for solar research. *Astron Nachr* **322**, 353–360 (2001).
16. Jiang P, Gan HQ, Yao R et al. FAST: the five-hundred-meter aperture spherical radio telescope. *Engineering* **28**, 21–25 (2023).
17. Leslie M. Webb space telescope hits its stride, dazzling astronomers. *Engineering* **22**, 3–6 (2023).
18. Tritschler A, Rimmele TR, Berukoff S et al. Daniel K. Inouye solar telescope: high-resolution observing of the dynamic sun. *Astron Nachr* **337**, 1064–1069 (2016).
19. Wang HM, Cao WD, Liu C et al. Witnessing magnetic twist with high-resolution observation from the 1.6-m new solar telescope. *Nat Commun* **6**, 7008 (2015).
20. Yurchyshyn V, Cao WD, Abramenko V et al. Rapid evolution of type II spicules observed in Goode solar telescope on-disk H_α images. *Astrophys J Lett* **891**, L21 (2020).
21. Tagle CD, Collados M, Lopez R et al. First light of the integral field unit of GRIS on the GREGOR solar telescope. *J Astron Instrum* **11**, 2250014 (2022).
22. Rao CH, Gu NT, Rao XJ et al. First light of the 1.8-m solar telescope-CLST. *Sci China Phys Mech Astron* **63**, 109631 (2020).
23. Gu NT, Li C, Cheng YT et al. Thermal control for light-weighted primary mirrors of large ground-based solar telescopes. *J Astron Telesc Instrum Syst* **5**, 014005 (2019).
24. Cai YF, Yang X, Xiang YY et al. The co-alignment of winged Hα data observed by the new vacuum solar telescope. *Res Astron Astrophys* **22**, 065010 (2022).
25. Matthews SA, Collados M, Mathioudakis M et al. The European solar telescope (EST). *Proc SPIE* **9908**, 990809 (2016).
26. Liu Z, Deng YY, Jin ZY et al. Introduction to the Chinese giant solar telescope. *Proc SPIE* **8444**, 844405 (2012).
27. Fu Y, Yuan S, Jin ZY et al. Polarization optical design of 8-meter Chinese giant solar telescope. *Acta Astron Sin* **64**, 8 (2023).
28. Fang C, Gu BZ, Yuan XY et al. 2.5m wide-field and high-resolution telescope. *Sci China Phys Mech Astron* **49**, 059603 (2019).
29. Hasan SS, Soltau D, Kärcher H et al. NLST: India's national large solar telescope. *Astron Nachr* **331**, 628–635 (2010).
30. Rao CH, Zhu L, Zhang LQ et al. Development of solar adaptive optics. *Opto-Electron Eng* **45**, 170733 (2018).
31. Berkefeld T, Schmidt D, Soltau D et al. The GREGOR adaptive optics system. *Astron Nachr* **333**, 863–871 (2012).
32. Femenía-Castella B, Cagigal MN, Cabrera MB et al. Adaptive optics at the European solar telescope: status and future developments. *Proc SPIE* **12185**, 121851Z (2022).
33. Rimmele TR, Radick RR. Solar adaptive optics at the national solar observatory. *Proc SPIE* **3353**, 72–81 (1998).
34. Shumko S, Gorceix N, Choi S et al. AO-308: the high-order adaptive optics system at big bear solar observatory. *Proc SPIE* **9148**, 914835 (2014).
35. Rao CH, Zhu L, Rao XJ et al. First generation solar adaptive optics system for 1-m new vacuum solar telescope at Fuxian solar observatory. *Res Astron Astrophys* **16**, 023 (2016).
36. Rao CH, Zhu L, Rao XJ et al. Instrument description and performance evaluation of a high-order adaptive optics system for the 1m new vacuum solar telescope at Fuxian solar observatory. *Astrophys J* **833**, 210 (2016).
37. Rao CH, Zhu L, Gu NT et al. A high-resolution multi-wavelength simultaneous imaging system with solar adaptive optics. *Astron J* **154**, 143 (2017).
38. Rimmele TR, Warner M, Keil SL et al. The *Daniel K. Inouye solar telescope*-observatory overview. *Sol Phys* **295**, 172 (2020).
39. Das S, Rao N, Phanindra DVS et al. SolarAccel: FPGA accelerated 2D cross-correlation of digital images: application to solar adaptive optics. *J Astrophys Astron* **45**, 16 (2024).
40. Zhu L, Gu NT, Chen SQ et al. Real time controller for 37-element low-order solar adaptive optics system at 1m new vacuum solar telescope. *Proc SPIE* **8415**, 84150V (2012).
41. Martin Y, Rodriguez-Ramos LF, García J et al. FPGA-bas*ed real time processing of the plenoptic wavefront sensor for the European solar telescope (EST). In 2010 VI Southern Programmable Logic Conference (SPL)* 87–92 (IEEE, 2010). http://doi.org/10.1109/SPL.2010.5483032.
42. Brusa G, Riccardi A, Wildi FP et al. MMT adaptive secondary: first AO closed-loop results. *Proc SPIE* **5169**, 26–36 (2003).
43. Salinari P, Sandler DG. High-order adaptive secondary mirrors: where are we. *Proc SPIE* **3353**, 742–753 (1998).
44. Johnson JA, Vaz A, Montoya M et al. Tuning the MAPS adaptive secondary mirror: actuator control, PID tuning, power spectra, and failure diagnosis. *Proc SPIE* **13149**, 131490H (2024).
45. Esposito S, Tozzi A, Ferruzzi D et al. First-light adaptive optics system for large binocular telescope. *Proc SPIE* **4839**, 164–173 (2003).
46. Esposito S, Tozzi A, Puglisi A et al. First light AO system for LBT: toward on-sky operation. *Proc SPIE* **6272**, 62720A (2006).
47. Riccardi A, Xompero M, Briguglio R et al. The adaptive secondary mirror for the large binocular telescope: optical acceptance test and preliminary on-sky commissioning results. *Proc SPIE* **7736**, 77362C (2010).
48. Arsenault R, Biasi R, Gallieni D et al. A deformable secondary mirror for the VLT. *Proc SPIE* **6272**, 62720V (2006).
49. Hibon P, Duhoux P. Improving the telescope guiding with field stabilization on the very large telescope/unit telescopes. *J Astron Telesc Instrum Syst* **9**, 027002 (2023).
50. https://giantmagellan.org/adaptive-secondary-optics/.
51. Hinz PM, Bowens-Rubin R, Baranec C et al. Developing adaptive secondary mirror concepts for the APF and W. M. Keck observatory based on HVR technology. *Proc SPIE* **11448**, 114485U (2020).
52. Guo YM, Chen KL, Zhou JH et al. High-resolution visible imaging with piezoelectric deformable secondary mirror: experimental results at the 1.8-m adaptive telescope. *Opto-Electron Adv* **6**, 230039 (2023).
53. Thomas S, Fusco T, Tokovinin A et al. Comparison of centroid computation algorithms in a Shack-Hartmann sensor. *Mon Not R Astron Soc* **371**, 323–336 (2006).
54. Mocci J, Busato F, Bombieri N et al. Efficient implementation of the Shack–Hartmann centroid extraction for edge computing. *J Opt Soc Am A* **37**, 1548–1556 (2020).
55. Zhou ZC, Zhang LQ, Zhu L et al. Comparison of correlation algorithms with correlating Shack–Hartmann wave-front images. *Proc SPIE* **10026**, 100261B (2016).
56. Ke ZB, Zhang LQ, Yang Y et al. Performance analysis and optimization of solar multiconjugate adaptive optics systems. *Mon*

Not R Astron Soc **530**, 307–317 (2024).

57. Yang Y, Zhang L, Yan N et al. Ground-layer adaptive optics for the 2.5 m wide-field and high-resolution solar telescope. *Res Astron Astrophys* **24**, 035018 (2024).
58. Cui ZJ, Qi WF, Liu YX. A fast image template matching algorithm based on normalized cross correlation. *J Phys Conf Ser* **1693**, 012163 (2020).
59. Liu SH, Zhong H, Li YQ et al. Fast and highly accurate zonal wavefront reconstruction from multi-directional slope and curvature information using subregion cancelation. *Appl Sci* **14**, 3476 (2024).
60. Mochi I, Goldberg KA. Modal wavefront reconstruction from its gradient. *Appl Opt* **54**, 3780–3785 (2015).
61. Noel ZA, Bukowski TJ, Gordeyev S et al. Shack-Hartmann wavefront reconstruction by deep learning neural network for adaptive optics. *Proc SPIE* **12693**, 126930G (2023).
62. Kolmogorov AN. Dissipation of energy in the locally isotropic turbulence. *Proc R Soc Lond A Math Phys Sci* **434**, 15–17 (1991).
63. Tyson RK. *Principles of Adaptive Optics* 2nd ed (Academic Press, Boston, 1998).
64. https://www.saiminprecision.com.
65. Wöger F, Uitenbroek H, Tritschler A et al. The ATST visible broadband imager: a case study for real-time image reconstruction and optimal data handling. *Proc SPIE* **7735**, 773521 (2010).

Acknowledgements

We gratefully acknowledge the financial support from the National Science Foundation of China (NSFC) (Grants No. 12293031 and No. 61905252), the National Science Foundation for Distinguished Young Scholars (Grant No. 12022308), and the National Key R&D Program of China (Grants No. 2021YFC2202200 and No. 2021YFC2202204). The research work for this thesis was conducted at the Institute of Optics and Electronics (IOE), Chinese Academy of Sciences (CAS), while the final writing and submission were completed at the College of Advanced Interdisciplinary Studies, National University of Defense Technology (NUDT). We sincerely appreciate the essential resources and equipment provided by my former affiliations including IOE, CAS, National Laborotatory on Adaptive Optics, and University of Chinese Academy of Sciences. We are deeply grateful to Associate Prof. Lanqiang Zhang, Xiaojun Zhang, Hong Liu, Yuntao Cheng, Kai Fang, Yangyi Liu, Benxi Yao, Zhiyong Wang for their invaluable technical assistance and to Prof. Wenhan Jiang for his insightful feedback during the preparation of this manuscript. We also extend our thanks to the anonymous reviewers for their constructive comments and suggestions, which have significantly improved the quality of this paper. Finally, we would like to express our heartfelt gratitude to our colleagues, friends, and family for their unwavering support and encouragement throughout this research journey.

Author contributions

All authors reviewed and commented on the manuscript. Naiting Gu proposed the methodology, directed the project, and organized both indoor and outdoor site experiments. Hao Chen, Ao Tang, and Xiaosong Wu conducted the theoretical analysis and numerical simulations. Carlos Quintero Noda generated the original solar photosphere layer images. Xinlong Fan designed and manufactured the 61-DSM. Naiting Gu, Changhui Rao, Yawei Xiao, and Zhenyu Zhang integrated the 600 mm ESAOT. Libo Zhong processed the observed solar images using the speckle method. Linhai Huang validated the feasibility of the proposed method. Yanrong Yang developed the data processing and adaptive optics (AO) control software. Naiting Gu, Xiaohu Wu, and Hao Chen wrote the initial draft of the manuscript. Xiaohu Wu and Zao Yi revised, reviewed, and polished the manuscript. Changhui Rao provided overall guidance and supervision for the research. Affiliation 1 is the Dr. Naiting Gu's current workplace, and the research was conducted while he was at affiliations 2, 3 and 4.

Competing interests

The authors declare no competing financial interests.

Supplementary information

Supplementary information for this paper is available at https://doi.org/10.29026/oea.2025.250025

Scan for Article PDF